minerals

MDPI

Article

Heterogeneous Nucleation and Growth of $CaCO_3$ on Calcite (104) and Aragonite (110) Surfaces: Implications for the Formation of Abiogenic Carbonate Cements in the Ocean

Hongmei Tang [1,2,3], Xiao Wu [1,2,3], Haiyang Xian [1,3,*], Jianxi Zhu [1,3], Jingming Wei [1,2,3], Hongmei Liu [1,3] and Hongping He [1,2,3]

1 CAS Key Laboratory of Mineralogy and Metallogeny/Guangdong Provincial Key Laboratory of Mineral Physics and Materials, Guangzhou Institute of Geochemistry, Chinese Academy of Sciences (CAS), Guangzhou 510640, China; tanghongmei@gig.ac.cn (H.T.); wuxiao@gig.ac.cn (X.W.); zhujx@gig.ac.cn (J.Z.); weijm@gig.ac.cn (J.W.); hmliu@gig.ac.cn (H.L.); hehp@gig.ac.cn (H.H.)

2 University of Chinese Academy of Sciences, Beijing 100049, China

3 Institutions of Earth Science, Chinese Academy of Sciences, Beijing 100029, China

* Correspondence: xianhaiyang@gig.ac.cn; Tel.: +86-20-85290569

Received: 3 March 2020; Accepted: 23 March 2020; Published: 25 March 2020

Abstract: Although near-surface seawater is supersaturated with $CaCO_3$, only a minor part of it is abiogenic (e.g., carbonate cements). The possible reason for such a phenomenon has attracted much attention in the past decades. Substrate effects on the heterogeneous nucleation and growth of $CaCO_3$ at various Mg^{2+}/Ca^{2+} ratios may contribute to the understanding of the origin of abiogenic $CaCO_3$ cements. Here, we used in situ atomic force microscopy (AFM), scanning electron microscopy (SEM), X-ray diffraction (XRD) and Raman spectroscopy to study the heterogeneous nucleation and growth of $CaCO_3$ on both calcite (104) and aragonite (110) surfaces. The results show that (1) calcite spiral growth occurs on calcite (104) surfaces by monomer-by-monomer addition; (2) the aggregative growth of aragonite appears on aragonite (110) surfaces through a substrate-controlled oriented attachment (OA) along the [001] direction, followed by the formation of elongated columnar aragonite; and (3) Mg^{2+} inhibits the crystallization of both calcite and aragonite without impacting on crystallization pathways. These findings disclose that calcite and aragonite substrates determine the crystallization pathways, while the Mg^{2+}/Ca^{2+} ratios control the growth rate of $CaCO_3$, indicating that both types of $CaCO_3$ substrate in shallow sediments and aqueous Mg^{2+}/Ca^{2+} ratios constrain the deposition of abiogenic $CaCO_3$ cements in the ocean.

Keywords: heterogeneous nucleation and growth; calcite (104) surface; aragonite (110) surface; substrate effect; Mg^{2+}/Ca^{2+} ratios; crystallization pathways; abiogenic $CaCO_3$ cements; in situ AFM

1. Introduction

The supersaturation of near-surface seawater is about six and four times higher than that with respect to calcite and aragonite, respectively, whereas a much smaller fraction of the total sedimentary $CaCO_3$ minerals is abiogenic [1], which contradicts traditional thermodynamics [2,3]. These abiogenic $CaCO_3$ minerals, composed of aragonite and high-magnesium calcite in shoal-shallow marine environments [4–6], typically form either as heterogeneously precipitated primary marine cements or through post-depositional and diagenetic reactions [1]. In order to further understand the lack of abiogenic $CaCO_3$ in the modern ocean, many efforts have been conducted to ascertain factors which affect the precipitation of abiogenic $CaCO_3$ [7–11].

The precipitation of abiogenic $CaCO_3$ correlates with aqueous chemistry [12]. The pH, temperature, P_{CO_2} and $a_{HCO_3^-}$ affect the saturation index (*SI*, which is defined as $SI = \log\Omega = \log(IAP/K_{sp})$, where Ω denotes saturation state, and *IAP* and K_{sp} represent activity product and solubility product, respectively) of solutions [13] and play key roles in determining the precipitate rate (r) of $CaCO_3$ polymorphs. The r is constrained by Ω, following the equation $r = k\ (\Omega - 1)^n$ [2]. In addition, the formation of $CaCO_3$ minerals is partly kinetically driven, i.e., calcite growth favors a low reaction rate, while aragonite and vaterite prefer to form in relatively fast reactions [14]. In addition, the precipitation of $CaCO_3$ (e.g., calcite) depends on the $a_{Ca^{2+}}/a_{CO_3^{2-}}$ of solutions. Due to the differences in the dehydration properties between Ca^{2+} and CO_3^{2-} and the geometry of calcite step kink sites, the step velocities of the obtuse and acute angled edges can reverse with the variation of $a_{Ca^{2+}}/a_{CO_3^{2-}}$ at a fixed *SI* [15–17]. On the other hand, impurity ions and molecules in solutions can also influence $CaCO_3$ precipitation. Inorganic anions (e.g., $PO_4^{3-}$and SO_4^{2-}) exert the impacts by competing with CO_3^{2-} for Ca^{2+} sites or incorporating in a crystal lattice [13]. Divalent metal cations, such as Mg^{2+}, Ba^{2+} and Sr^{2+}, inhibit calcite growth by step pining, incorporation or kink blocking [18–21]. Similarly, soluble organic molecules (such as humate, fulvate, citrate and polyfunctional aromatic acids) inhibit the precipitation of aragonite by the modification of functional groups in these additives [11,22,23].

The surface properties of the growth substrate are another factor affecting the precipitation of abiogenic $CaCO_3$ [24–27]. The surface charge of an inorganic substrate relates to the growth of $CaCO_3$ polymorphs. Metastable $CaCO_3$ phases (e.g., aragonite or vaterite) are favored by negatively charged substrates, whereas positively charged substrates contribute to the formation of the stable $CaCO_3$ phase (i.e., calcite) [28]. In addition, the lattice mismatch between substrates and surface precipitates is also vital in the growth of abiogenic $CaCO_3$ [29]. Based on classical nucleation theory, the energy barrier (ΔG_C) to form a critical nucleus is positively correlated with γ^3 ($\Delta Gc \propto \gamma^3/(-RT\ln\sigma)^2$, where γ denotes the interfacial free energy, σ the supersaturation, and R and T represent gas constant and Kelvin temperature, respectively [30]. The precipitation rate is subsequently controlled by the lattice mismatch, because a larger lattice mismatch leads to a higher ΔG_C [31].

Abiogenic $CaCO_3$ cements tend to overgrow on shoal-shallow calcium carbonate-rich sediments [32]. Different types of $CaCO_3$ inorganic substrate should be taken into consideration, to study the precipitation of abiogenic $CaCO_3$ cements. The substrate effects of $CaCO_3$ have been found to control the mineralogical properties of carbonate cements [7,13], and plenty of works have also been conducted on the heterogeneous nucleation and growth of $CaCO_3$ on calcite and aragonite seeds [33–35]. However, little attention has been paid to the internal mechanism and crystallization pathways of $CaCO_3$ precipitates in these systems. Although the precipitation of $CaCO_3$ on calcite (104) surfaces has been well documented [3,23,36,37], it may not represent the formation of abiogenic aragonite cements, due to the distinct surface properties of the two polymorphs [38]. Additionally, there are some controversies regarding aragonite nucleation and growth in Mg^{2+}-bearing solutions. Mg^{2+}-induced inhibition was reported in both nucleation and growth [39], whereas either inhibition [33] or non-inhibition [40] was merely found in the growth processes. Therefore, the evolution and mechanism of heterogeneous nucleation and growth of both calcite and aragonite at the nanoscale on $CaCO_3$ substrates in Mg^{2+}-bearing solutions with different concentrations should be investigated, to deeply understand the formation of abiogenic carbonate cements in the ocean.

In this study, we used AFM, SEM, XRD and Raman spectroscopy to investigate how calcite (104) and aragonite (110) substrates affect the heterogeneous nucleation and growth of $CaCO_3$ under different solution supersaturations at pH = 8.0 ± 0.1. Since Mg^{2+} is a chief modifier for $CaCO_3$ precipitation in sedimentary environments, we altered the Mg^{2+}/Ca^{2+} ratios from 0 to 3 in the growth experiment. We observed that both the mineral phases and crystallization pathways of $CaCO_3$ precipitated on different types of $CaCO_3$ substrates are disparate. In addition, the precipitation rates of $CaCO_3$ generated on calcite and aragonite substrates are negatively correlated to Mg^{2+}/Ca^{2+} ratios. These findings reveal the different crystallization processes of $CaCO_3$ grown on calcite (104) and aragonite (110) surfaces, providing a new perspective on the origin of abiogenic $CaCO_3$ cements in the ocean.

2. Materials and Methods

2.1. Sample Preparation

An Iceland spar (from Guizhou, China) was cleaned using ethanol and deionized water (resistivity = 18.2 MΩ cm^{-1}). Then, fresh calcite (104) surfaces (2 × 2 × 1 mm^3) were prepared by scalpel cutting along the cleavage plane. Additionally, a diamond wire cutter (STX-202A, Kejing Auto-instrument Co., Ltd., Shenyang, China) was used to slice aragonite (110) surfaces (2 × 2 × 1 mm^3) from single crystals (from Morocco). To obtain polished aragonite (110) surfaces, a Leica SP1600 (Leica, Wetzlar, Germany) saw microtome was employed. Since polished aragonite (110) surfaces would enhance the growth rate of $CaCO_3$ by the increase in surface defects (which will reduce the energy barrier (ΔG_C) to form a critical nucleus, and the number of nanoparticles will increase after increasing surface defects, thus causing the increase in growth rate), we used them in the next experiments to elevate experimental efficiency. Next, 15 mL acetone was used to wash these polished (110) surfaces through ultrasonic bathing for 1 h, and then these (110) surfaces were taken out from acetone and dried with pure N_2. Afterwards, these prepared calcite (104) and aragonite (110) samples were glued onto steel pucks with wax for AFM experiments.

2.2. Solution Preparation

High-purity $CaCl_2$, $MgCl_2$, $NaHCO_3$, NaCl (purchased from Aldrich and Macklin) and deionized water were used to prepare solutions with different Mg^{2+}/Ca^{2+} ratios (0 and 3) and saturation indexes, with respect to calcite and aragonite (i.e., $SI_{calcite}$ and $SI_{aragonite}$), based on Visual MINTEQ [41] calculations (Table 1). Since the $SI_{calcite}$ is 0.13 greater than $SI_{aragonite}$ ($SI_{calcite} = SI_{aragonite} + 0.13$) in the same solution, we only used the former to label saturation states of solutions. Solution chemistry in the system is constrained by the amounts of $[Mg^{2+}]$, $[Ca^{2+}]$, $\sum CO_2$, pH, and ionic strength (*IS*). The pH was maintained at 8.0 ± 0.1, and the *IS* was controlled up to 0.10 M (to avoid the coverage of substrates by too much NaCl, we did not used the salinity of seawater). All solutions were freshly prepared before the growth experiment, to prevent the precipitation of supersaturated solutions. Before introducing growth solutions, the solution with $SI_{calcite} = 0.07$ was injected into the fluid cell for at least one hour to make the surface of samples flatter. Based on solution chemistry, equilibriums in chemical reactions were taken into consideration as the following.

$$Mg(OH)_2 + 2H^+ \rightarrow Mg^{2+} + 2H_2O \; K_{sp\text{-}1} \quad (1)$$

$$MgCO_3{\cdot}3H_2O \rightarrow Mg^{2+} + CO_3{}^{2-} + 3H_2O \; K_{sp\text{-}2} \quad (2)$$

$$H_2CO_3 \rightarrow H^+ + HCO_3{}^- \; K_{a1} \quad (3)$$

$$HCO_3{}^- \rightarrow H^+ + CO_3{}^{2-} \; K_{a2} \quad (4)$$

Table 1. Compositions and solution chemistry calculated by Visual MINTEQ.

SI_{cal}	Mg^{2+}/Ca^{2+}	$MgCl_2$ (mM)	$CaCl_2$ (mM)	$NaHCO_3$ (mM)	NaCl (mM)	pH	*IS* (M)
0.50	0	0	1.00	10.00	90.00	7.98	0.10
	3	3.15	1.05	10.50	85.00	7.95	0.10
0.83	0	0	1.50	15.00	89.00	7.97	0.11
	3	4.65	1.55	15.50	70.00	7.94	0.10
1.05	0	0	2.00	20.00	85.00	7.96	0.11
	3	6.30	2.10	21.00	60.00	7.92	0.10

From the definition of K_{sp}, we derived

$$\log(Mg^{2+}) = -2pH + \log K_{sp\text{-}1} \quad (5)$$

$$\log(Mg^{2+}) = \log(K_{sp\text{-}2}[1+10^{-pH}/K_{a2} + 10^{-2pH}/ K_{a1}K_{a2}]/\Sigma CO_2) \quad (6)$$

where (Mg^{2+}) represents the activity of Mg^{2+}, and $\sum CO_2$ is the total concentration of carbonate species. Equations (5) and (6) define the stability fields of brucite and nesquehonite in the two-dimensional stability diagram of log (Mg^{2+}) – pH, respectively (Figure 1). The concentrations of $\sum CO_2$ ($10 \times [Ca^{2+}]$) and $[Ca^{2+}]$ ($1/3 \times [Mg^{2+}]$) in these equations were determined based on additive amounts.

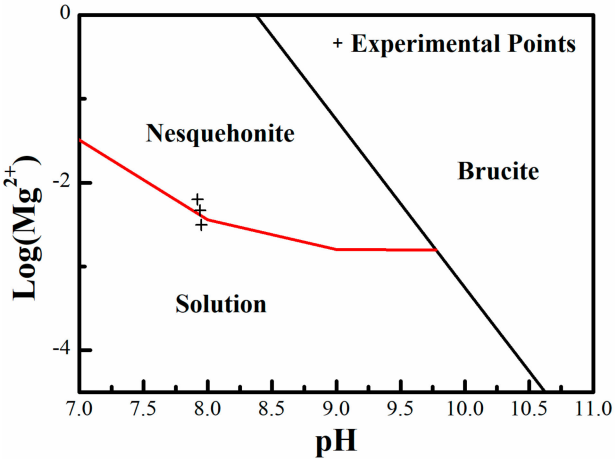

Figure 1. Stability diagram of brucite and nesquehonite with respect to Mg^{2+} activity and solution pH. The cross symbols mark the compositions of experimental solutions in this study.

2.3. Growth Experiments Measured by In Situ AFM

A Bruker Nanoscope IV Scanning Probe Microscope equipped with a flow-through fluid cell and Si_3N_4 cantilevers was used to collect AFM images. The operational process was similar to that in our previous study [42]. After flatjaw pinchcocks were turned on, a flowing system formed between the O-ring installed on the fluid cell and sample. The flow rate of solutions was performed at 550 uL/min throughout the in situ growth experiment.

2.4. SEM, XRD and Raman Spectroscopy Analysis

SU8010 cold field emission SEM (FESEM, Hitachi, Japan), equipped with energy dispersive X-ray spectroscopy (EDS) (AMETEK-EDAX, Mahwah, NJ, USA), was utilized to observe surface morphologies and chemical compositions after growth under different conditions. In addition, mineral phases precipitated on the surfaces of substrates were analyzed by a Rigaku DMAX Rapid II X-ray diffraction system (Rigaku, Tokyo, Japan) (Mo$K\alpha$ radiation), at 50 mV and 30 mA. A Micro-confocal Raman spectrometer (in Via, Renishaw-RM 2000 (Renishaw, Gloucestershire, UK)) at 532 nm laser extinction was also used to identify precipitates formed on these substrates.

3. Results

3.1. The Heterogeneous Nucleation and Growth of $CaCO_3$ on Calcite (104) Surfaces

Under $Mg^{2+}/Ca^{2+} = 0$ conditions, spiral growth of calcite, with the monomolecular of growth hillock around 3.1 Å, is observed as the solution system reaches a steady-state (Figure S1a–c and Figure 2a). The morphology of growth hillock is a rhombus which consists of two acute and obtuse angles (Figure S1d). The terrace width (λ) of steps is negatively correlated to the increase in solution $SI_{calcite}$ (Figure S1a–c) [3]. When the $SI_{calcite}$ of the solutions is equal to 0.50, 0.83 and 1.05, the λ values

of obtuse steps are 175.43, 171.25 and 123.60 nm, respectively, while those of acute steps are 77.33, 74.25 and 62.80 nm, respectively. In addition, the calcite (104) surface after growing in the solution at $SI_{calcite}$ = 1.05 and Mg^{2+}/Ca^{2+} = 0 was characterized by SEM and EDS. We observed that these growth hillocks are covered by a layer of $CaCO_3$ crust, which is smooth and evenly distributed (Figure S1e–g).

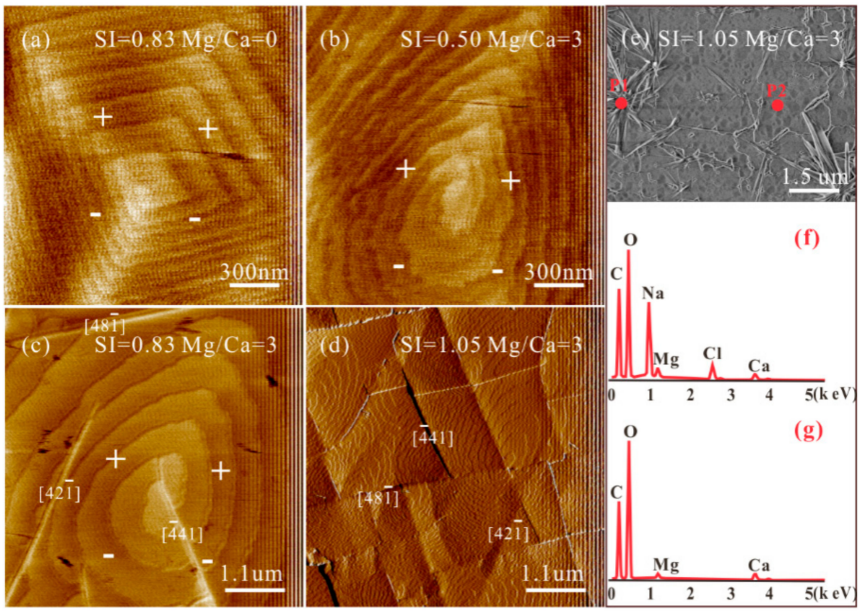

Figure 2. AFM results of the calcite (104) cleavage surfaces in solutions at pH = 8.0 ± 0.1 of height images with (**a**) $SI_{calcite}$ = 0.83, Mg^{2+}/Ca^{2+} = 0; (**b**) $SI_{calcite}$ = 0.50, Mg^{2+}/Ca^{2+} = 3; (**c**) $SI_{calcite}$ = 0.83, Mg^{2+}/Ca^{2+} = 3; and deflection image with (**d**) $SI_{calcite}$ = 1.05, Mg^{2+}/Ca^{2+} = 3; and (**e**) SEM image with $SI_{calcite}$ = 1.05 and Mg^{2+}/Ca^{2+} = *3*, and (**f**) and (**g**) represent EDS analysis of P1 and P2 labeled in (**e**), respectively.

The effects of $SI_{calcite}$ and Mg^{2+}/Ca^{2+} ratios on calcite growth were investigated. Under the condition of Mg^{2+}/Ca^{2+} = 3 and $SI_{calcite}$ = 0.50, a tear-drop shaped morphology of growth hillock emerges on the calcite (104) surface (Figure 2b). With a modest increase in $SI_{calcite}$ to 0.83, a sudden buckling of terraces cutting through multiple steps forms. These buckled terraces possess ridges in the direction of $[42\bar{1}]$, $[\bar{4}41]$ and $[48\bar{1}]$, segmenting the calcite surface into multiple area blocks (Figure 2c). Continuously elevating the $SI_{calcite}$ to 1.05, the number of segments increases on the calcite (104) surface (Figure 2d). SEM images and EDS spectra of the calcite (104) surface after growing at $SI_{calcite}$ = 1.05 and Mg^{2+}/Ca^{2+} = 3 were acquired (Figure 2e). Except for the needlelike NaCl crystals produced on the substrate, the other precipitates are $Ca_{(1-x)}Mg_xCO_3$ with segmented surfaces. We also used EDS to semi-quantify the Mg^{2+} contents in these overgrowths precipitated on calcite (104) substrates in the solution at Mg^{2+}/Ca^{2+} =*3* and $SI_{calcite}$ = 1.05, discovering that it ranges from 24.68 at% (P2) to 43.20 at% (P1).

3.2. The Heterogeneous Nucleation and Growth of $CaCO_3$ on Aragonite (110) Surfaces

Under conditions of Mg^{2+}/Ca^{2+} = 0, the heterogeneous nucleation and growth of $CaCO_3$ on aragonite (110) substrates were investigated at low, intermediate, and high $SI_{calcite}$. At $SI_{calcite}$ = 0.50, nanoparticles gradually precipitated on the aragonite (110) growth surface. These nanoparticles increase in size and number with time (Figure 3). After 190 min, we observed that these individual nanoparticles elongate along the $[\bar{1}10]$ direction, while the aggregates of these nanoparticles form crystals extending along the [001] direction (Figure 3f), indicating a substrate-controlled OA growth pathway. Nevertheless, we can only observe columnar crystals extending along the [001] direction on polished aragonite (110) surfaces, without discovering the solid-solid interfaces among these

nanoparticles in the solution at $SI_{calcite}$ = 0.50 (Figure 4). Increasing $SI_{calcite}$ to 0.83, the aggregation rate of nanoparticles is enhanced (Figure 5). Crusts composed of nanoparticles cover the substrate after 5 min (Figure 5c), and these crusts rapidly evolve to elongated columnar crystals (Figure 5c–h). Further increasing $SI_{calcite}$ to 1.05, the phenomena are generally similar to what is observed in the solution at $SI_{calcite}$ = 0.83, except that crusts only sporadically cover the substrate (Figure S2).

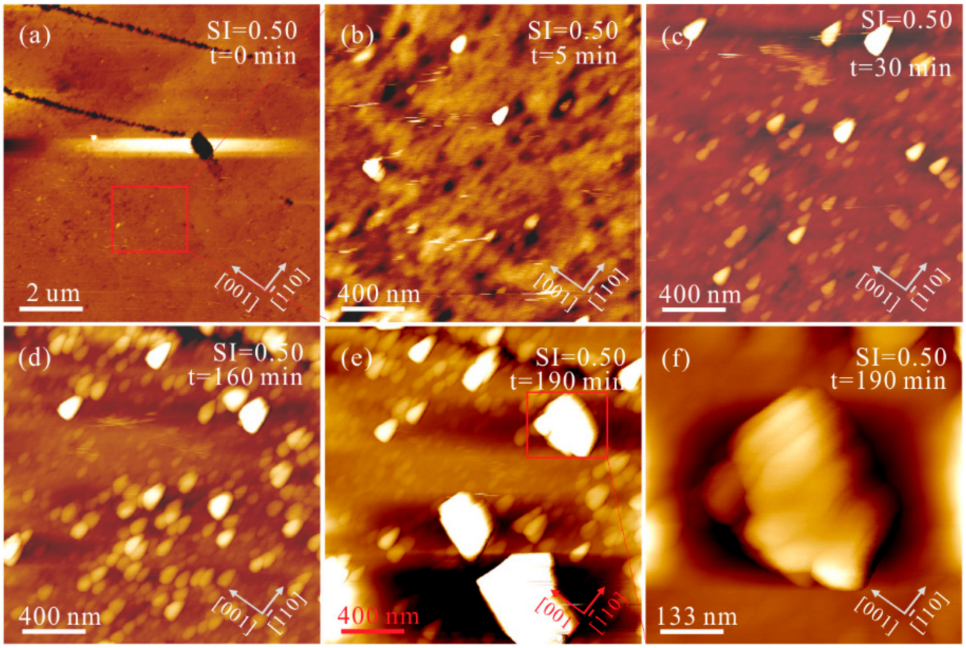

Figure 3. AFM height images of the aragonite (110) growth surface in solutions (Mg^{2+}/Ca^{2+} = 0, $SI_{calcite}$ = 0.50) under flowing conditions at pH = 8.0 ± 0.1 for (**a**) 0, (**b**) 5, (**c**) 30, (**d**) 160 and (**e**) 190 min, and (**f**) denotes the same zone marked with red box in (**e**). The region marked with the red box in (**a**) represents the same zones in (**b**–**e**).

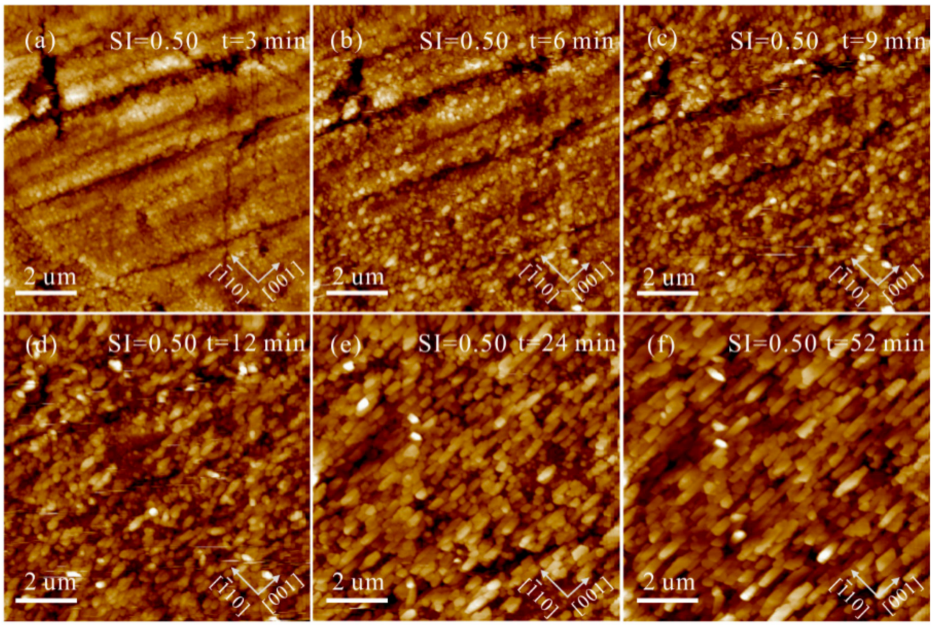

Figure 4. AFM height images of the polished aragonite (110) surface in solution (Mg^{2+}/Ca^{2+} = 0, $SI_{calcite}$ = 0.50) under static conditions at pH = 8.0 ± 0.1 for (**a**) 3, (**b**) 6, (**c**) 9, (**d**) 12, (**e**) 24 and (**f**) 52 min.

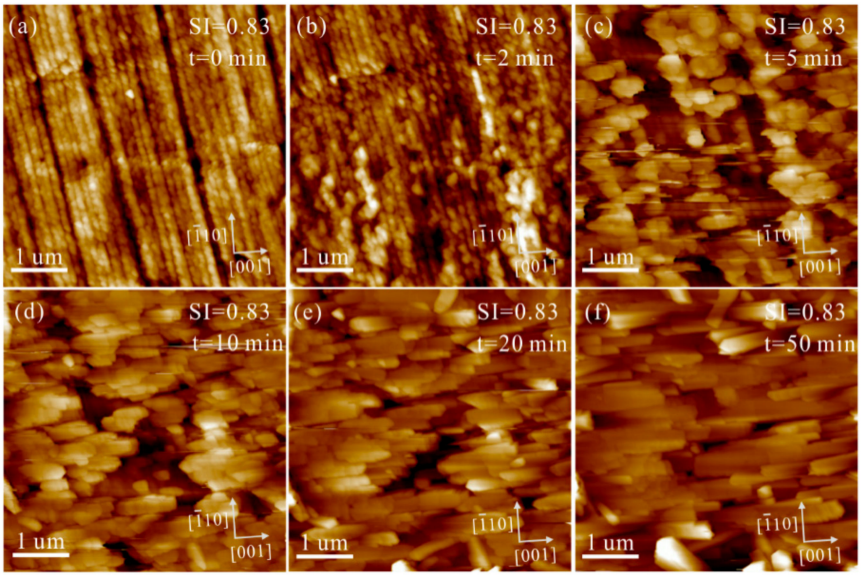

Figure 5. AFM height images of the polished aragonite (110) surface in solution (Mg^{2+}/Ca^{2+} = 0, $SI_{calcite}$ = 0.83) under flowing conditions at pH = 8.0 ± 0.1 for (**a**) 0, (**b**) 2, (**c**) 5, (**d**) 10, (**e**) 20 and (**f**) 50 min.

SEM was used to observe aragonite (110) surfaces after the heterogeneous nucleation and growth of $CaCO_3$ in solutions with different $SI_{calcite}$. The size and morphology of these crystals are identical, while the orientation of crystals in the lower and upper layers is disparate. Crystals in the lower layer have their *c* axes parallel to aragonite (110) substrates, whereas those in the upper layer have their *c* axes perpendicular to the substrates (Figure 6). The surfaces of these crystals are generally smooth, only with local cracks and holes (as indexed by the red arrows in Figure 6f,h). In addition, nanoparticles are observed from the broken parts and a few crystal surfaces (as indexed by the red arrows in Figure 6e,f).

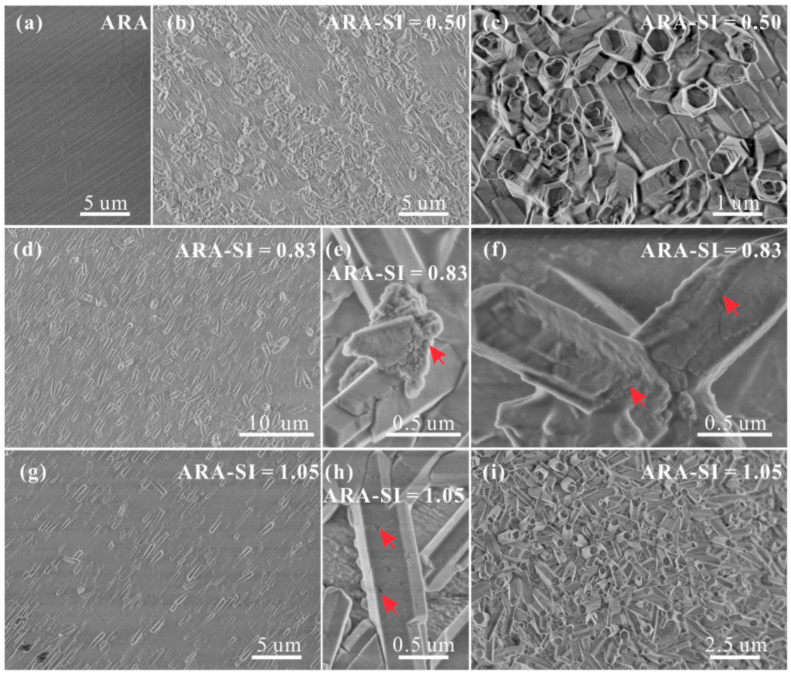

Figure 6. SEM images of (**a**) the polished aragonite (110) surface, and polished aragonite (110) surfaces after growing in solutions with Mg^{2+}/Ca^{2+} = 0 and (**b**,**c**) $SI_{calcite}$ = 0.50; (**d**–**f**) $SI_{calcite}$ = 0.83; (**g**–**i**) $SI_{calcite}$ = 1.05.

The heterogeneous nucleation and growth of $CaCO_3$ on polished aragonite (110) substrates were investigated in solutions under $Mg^{2+}/Ca^{2+} = 3$. The aggregation process of nanoparticles, which is similar to that without Mg^{2+} addition, can be captured by in situ AFM (Figure 7). Meanwhile, the interfaces among these nanoparticles are extremely obvious, even after 180 min (as indexed by the red arrows in Figure 7h). Increasing $SI_{calcite}$ to 0.83 and eventually to 1.05, the aggregation rate of nanoparticles soars, while their solid-solid interfaces are still preserved (Figure 8 and Figure S3).

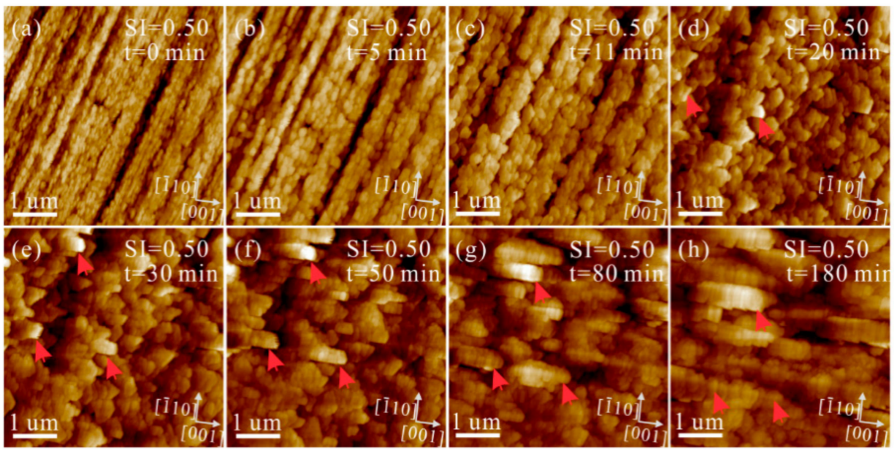

Figure 7. AFM height images of the polished aragonite (110) surface in the solution ($Mg^{2+}/Ca^{2+} = 3$, $SI_{calcite} = 0.50$) under flowing conditions at pH = 8.0 ± 0.1 for (**a**) 0, (**b**) 5, (**c**) 11, (**d**) 20, (**e**) 30, (**f**) 50, (**g**) 80 and (**h**) 180 min.

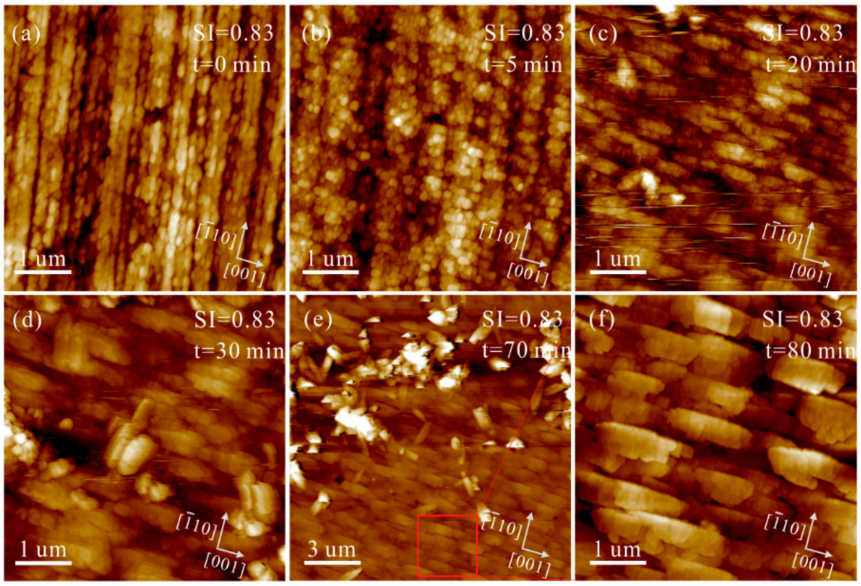

Figure 8. AFM height images of the polished aragonite (110) surface in the solution ($Mg^{2+}/Ca^{2+} = 3$, $SI_{calcite} = 0.83$) under flowing conditions at pH = 8.0 ± 0.1 for (**a**) 0, (**b**) 5, (**c**) 20, (**d**) 30 and (**e**) 70 min, and (**f**) represents the same zone marked with red box in (**e**), which grows for 80 min.

The surfaces after growing in supersaturated solutions with $Mg^{2+}/Ca^{2+} = 3$ were analyzed by SEM. Although some rhombohedral particles form on these substrates, tower-like and elongated columnar crystals are major precipitates (Figure 9a,c,e). Additionally, some crystals with smooth surfaces generate around these tower-like crystals (Figure 9c,f). The surface roughness of these tower-like crystals, positively correlated with the increase in $SI_{calcite}$, is greater than that of crystals precipitated in Mg^{2+}-free solutions (Figure 9b,d,f).

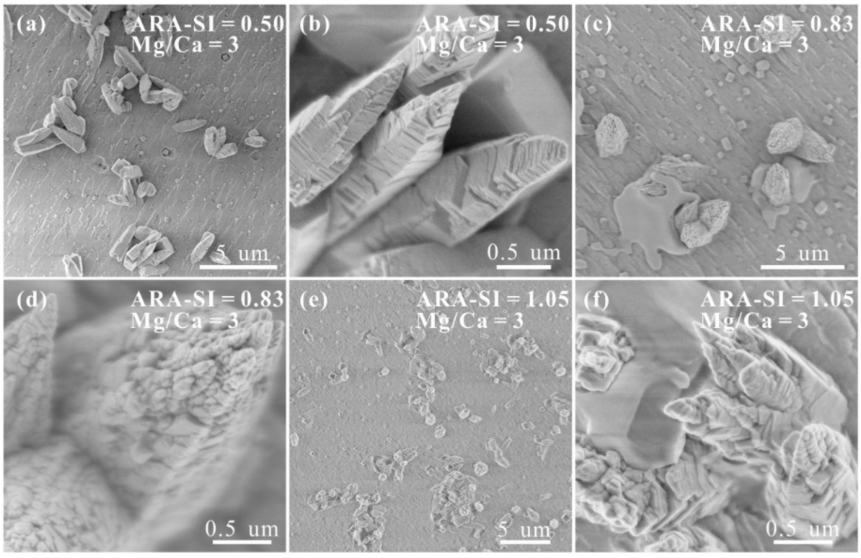

Figure 9. SEM images of the polished aragonite (110) surfaces after growing in solutions with Mg^{2+}/Ca^{2+} = 0 and (**a**,**b**) $SI_{calcite}$ = 0.50; (**c**,**d**) $SI_{calcite}$ = 0.83; (**e**,**f**) $SI_{calcite}$ = 1.05.

3.3. Mineral Phases of $CaCO_3$ Dependent on Calcite (104) and Aragonite (110) Substrates

Mineral phases of $CaCO_3$ precipitates have been identified by XRD and Raman analyses. The XRD results show that calcite and aragonite tend to precipitate on calcite (104) and aragonite (110) substrates, respectively (Figure 10a). Under our experimental conditions, the addition of Mg^{2+} does not induce the formation of protodolomite, dolomite, hydromagnesite (e.g., nesquehonite) or magnesite (Figure 10b). In addition, the relative intensity of XRD reflections is distinct after $CaCO_3$ grows on calcite (104) and aragonite (110) substrates in different solutions. The Raman results demonstrate that the mineral phase of aragonite formed on aragonite (110) substrates will not be affected by solution $SI_{calcite}$ (Figure 11a). In addition, we cannot observe the obvious change in mineral phase under Mg^{2+}/Ca^{2+} = 3 compared with that under Mg^{2+}/Ca^{2+} = 0 (Figure 11b).

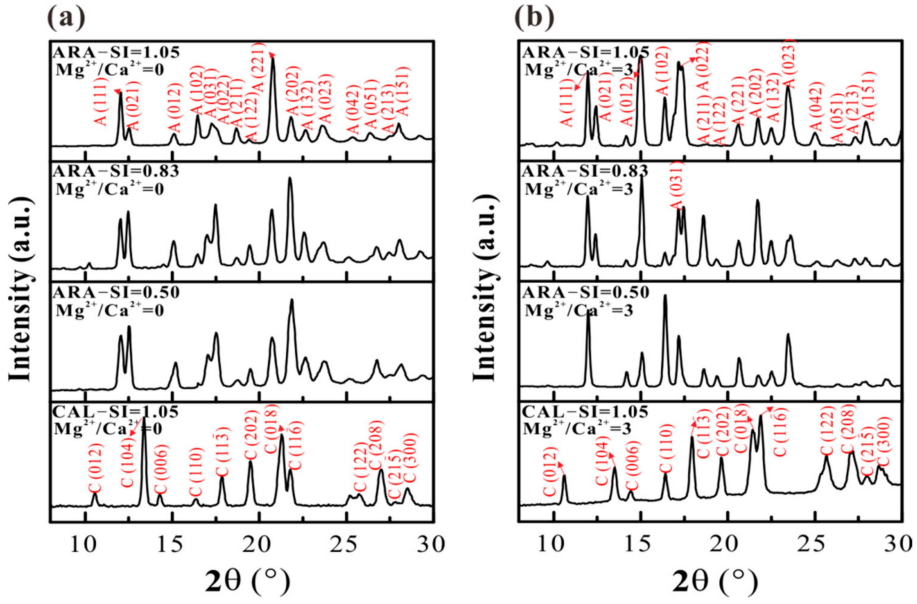

Figure 10. XRD patterns of the calcite (104) and aragonite (110) substrates after growing in solutions at $SI_{calcite}$ = 0.50 – 1.05 with (**a**) Mg^{2+}/Ca^{2+} = 0, and (**b**) Mg^{2+}/Ca^{2+} = 3.

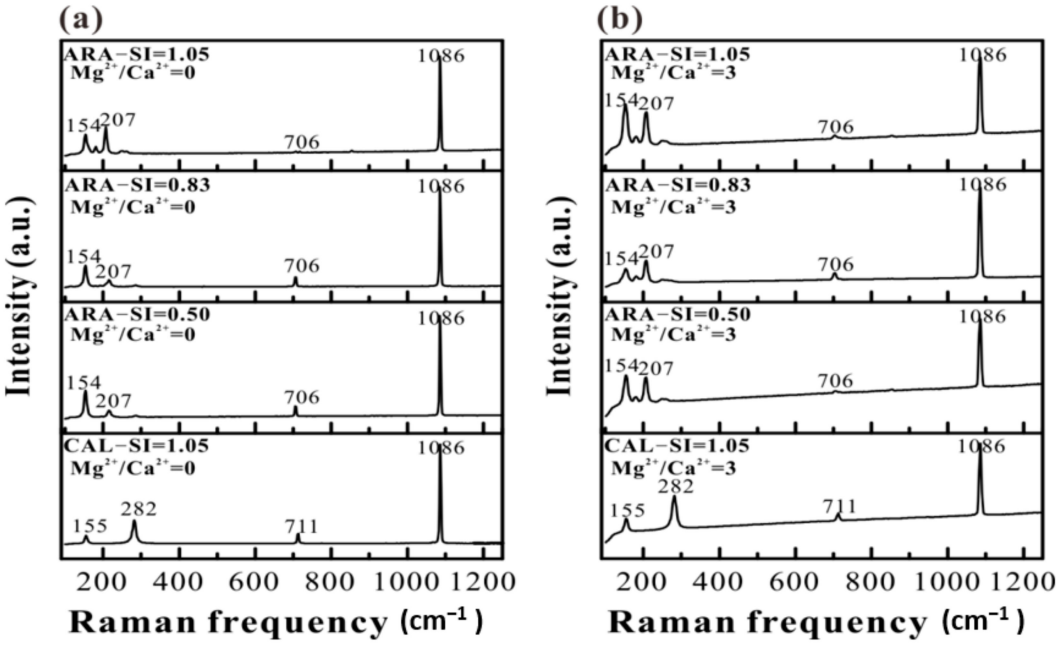

Figure 11. Raman spectra of the calcite (104) and aragonite (110) substrates after growing in solutions at $SI_{calcite}$ = 0.50–1.05 with (**a**) Mg^{2+}/Ca^{2+} = 0, and (**b**) Mg^{2+}/Ca^{2+} = 3.

4. Discussion

4.1. Different Crystallization Pathways of Heterogeneous Nucleation and Growth of $CaCO_3$ on Calcite (104) and Aragonite (110) Surfaces

Classical and nonclassical nucleation and growth theories play critical roles in understanding the formation of minerals. The former stresses the whole processes, including the diffusion of monomers from solution to solid surfaces, the transformation of monomers from surfaces to active sites, and eventually the growth of crystals [43]. The latter emphasizes the formation and aggregation of precursors in the solution [44]. Based on our results, $CaCO_3$ crystals formed on calcite (104) surfaces crystallize by spiral growth, and these $CaCO_3$ crystals are not typical rhombohedral calcite particles. In contrast, nanoparticles are initially generated on aragonite (110) surfaces, and then followed by OA and finally form elongated columnar crystals. These crystals precipitated on aragonite (110) surfaces are divided into two layers. The crystals in the first layer are arranged with their *c* axes parallel to the substrate, while those in the second layer are perpendicular to the substrate. These two different orientations of crystals can be ascribed to the limitation of growth space [45]. The growth of crystals in the second layer is constrained by gaps between crystals formed in the first layer, leading to vertical extension. The SEM results show that the crystals are composed of nanoparticles, which is evidence of particle aggregation. Therefore, we proposed that the heterogeneous nucleation and growth of $CaCO_3$ on calcite (104) surfaces are in accordance with classical nucleation and growth theory (i.e., monomer-by-monomer addition), while those on aragonite (110) surfaces conform to nonclassical nucleation and growth theory (i.e., precursor attachment).

The results of XRD and Raman analyses demonstrate that the $CaCO_3$ precipitated on calcite (104) surfaces is calcite, whereas that formed on aragonite (110) surfaces is aragonite, which is attributed to the complete lattice match between minerals with identical phases [31,46]. The relative intensity of XRD reflections, as well as Raman frequencies, of the same type of substrate grown in different solutions is distinct, which is ascribed to different orientations of $CaCO_3$ precipitates on local surfaces. Additionally, the surface roughness of aragonite (110) is greater than that of the calcite (104) surfaces in this study, causing the drop in local supersaturation on aragonite (110) surfaces and the eventual formation of sporadic rhombohedral $CaCO_3$ (probably calcite) (Figure 9).

The crystallization pathways of calcite and aragonite on calcite (104) and aragonite (110) surfaces in this study are similar to those precipitated in homogeneous systems [47–49]. Hence, the differences in crystallization pathways between calcite and aragonite may be decided by their own crystalline behaviors. A previous study proposed that the binding force of rhombic crystals in 3D directions is identical, while that of prismatic crystals along the *c* axes is greater than that in both the *a* and *b* directions [50], which perfectly explains our AFM observations that aggregates of nanoparticles formed on aragonite (110) surfaces extend along the *c* axes.

4.2. Effects of Mg^{2+} and Saturation States on the Heterogeneous Nucleation and Growth of $CaCO_3$ on Calcite (104) and Aragonite (110) Surfaces

Both Mg^{2+}/Ca^{2+} ratios and solution supersaturations impact $CaCO_3$ growth. On the one hand, when Mg^{2+}/Ca^{2+} ratios increase from 0 to 3, the spiral growth of calcite is inhibited. Sethmann et al. (2010) observed the segmentation of Mg-calcite thin films on calcite (104) surfaces, and they discovered that the premise of ridge formation is to break through the critical thickness (about 12 nm), which signifies the release of compress stress when the thickness exceeds the critical value [51]. Due to the ionic radius of Mg^{2+} (0.86 Å) being about 30% smaller than that of Ca^{2+} (1.14 Å) [52], the Mg^{2+} substitution of Ca^{2+} will increase the compress stress. This stress will be released through layer buckling and breaking along the $[\bar{4}41]$, $[48\bar{1}]$ and $[42\bar{1}]$ directions [37].

On the other hand, Mg^{2+} also decreases the crystallization rate of aragonite. The magnitude of the kinetic coefficient (β) is controlled by the density of kink sites along the step (n_k) and the net probability of attachment to a site ((exp(E_k/kT), where k and T represent the Boltzmann constant and Kelvin temperature, respectively, and E_k denotes an effective barriers to attachment at a kink). Namely, $\beta \sim n_k$ exp(-E_k/kT) [53]. As many nanoparticles form on aragonite (110) surfaces, the n_k reaches the maximum value. Therefore, the exp(E_k/kT), instead of the n_k, is the major factor affecting β. Since the exp(E_k/kT) is related to the desolvation of cations, which is the rate-limiting step during $CaCO_3$ growth, the dynamics of particle aggregation would be restricted when solvation layers are strongly bounded [44]. The desolvation of Mg^{2+} is more difficult than that of Ca^{2+}, resulting in a slower crystallization rate of aragonite in Mg^{2+}-bearing solutions. As a result, the OA of nanoparticles aggregates along the [001] direction is much easier to be observed.

As supersaturations of solutions are positively correlated with growth rates of $CaCO_3$ [2], the aggregation rate of nanoparticles is obviously accelerated in solutions with higher supersaturation. However, the solid-solid interfaces among nanoparticles are still obvious under these conditions (Figure 8 and Figure S3), indicating that it is difficult to eliminate the inhibition of Mg^{2+} on the crystalline rate of $CaCO_3$, even in highly supersaturated solutions (from 0.50 to 1.05).

4.3. Comparison with Previous Studies

The *IS* and Mg^{2+}/Ca^{2+} ratios in our study are different with those in seawater and some previous studies; nevertheless, our results can be reasonably inferred to $CaCO_3$ precipitation in the ocean. Although the *IS* in our study (0.1 M) is much lower than that in seawater (*IS* = 0.7 M), Zhong and Mucci (1989) discovered that salinity variations alone will not significantly affect both the precipitation rates and overgrowth compositions of calcite and aragonite [35]. In addition, the critical Mg^{2+}/Ca^{2+} ratios favoring calcite or aragonite ranges from 1.5 to 2 [30,54], and when the Mg^{2+}/Ca^{2+} ratios in solutions are less than 7.5, the distribution coefficients of Mg^{2+}, both in mineral overgrowths and on their adsorbed layers, are positively correlated with Mg^{2+}/Ca^{2+} ratios of solutions [34]. Therefore, the experimental consequences obtained at Mg^{2+}/Ca^{2+} = 3 in this study can represent those in real seawater at Mg^{2+}/Ca^{2+} = 5.

4.3.1. Calcite Precipitation

The growth features of calcite in Mg^{2+}-free solutions (Figure S1a–c) are used for comparison with previous studies. We discovered that the differences in terrace width between obtuse and acute steps ($\Delta\lambda$) are 98.10, 97.00 and 60.80 nm at $SI_{calcite}$ = 0.50, 0.83 and 1.05, respectively. Since the λ of steps is negatively related to the step velocity [3], the difference in step velocity between obtuse and acute steps is positively correlated with solution $SI_{calcite}$ at $a_{Ca^{2+}}/a_{CO_3^{2-}}$ = 10, which is consistent with previous experimental and fitting data [16,17]. Additionally, when we convert $SI_{calcite}$ = 0.50 to supersaturation σ ($SI_{calcite}$ = log(exp(σ))), the σ value is equal to 1.15, and we found that the λ values of obtuse and acute steps under our experiment (175.43 and 77.33 nm) are slightly higher than those (152.67 and 75.00 nm) reported by Wasylenki et al. (2005), which may be caused by the minor differences of $a_{Ca^{2+}}/a_{CO_3^{2-}}$ [55].

The inhibiting effect of Mg^{2+} on the spreading rate of the calcite growth hillock in this study is similar to that in previous studies. Two basic impurity models for the inhibiting effect of Mg^{2+} on the growth of calcite (104) surfaces are widely accepted. One is step pinning [56,57], while the other is incorporation [57,58]. In the former model, the adsorption of Mg^{2+} on step sites is a reversible process, while Mg^{2+} incorporated into the calcite lattice cannot be reversed in the latter. Based on the inhibiting effect of a newly formed monolayer on the growth of subsequent monolayers, Astilleros et al. (2010) proposed a new solid solution-aqueous solution model, providing an explanation for the formation of "dead zones" in the step pinning model [59]. According to our AFM results (Figure 2b–d), these three models probably coexist. The Mg^{2+} ions can pin at non-specific sites, while only incorporated at specific sites. Additionally, the surface properties of the first monolayer formed on the calcite (104) surface would be altered upon Mg^{2+} incorporation, causing the growth inhibition of subsequent monolayers. Some researchers have declared that the incorporation of Mg^{2+} into calcite leads to the increase in mineral solubility, which contributes to aragonite precipitation [33]. However, based on the thermodynamic simulation, the increase of surface energy by incorporating Mg^{2+} into calcite is the main reason for the rise of the energy barrier (ΔG_C) to form a critical nucleus of calcite [30]. Similarly, the spreading rates of calcite steps are negatively correlated with the free energy ($\Delta g_{\pm}$) ($\Delta g_{\pm} = -(L/b)\Delta\mu + 2c\langle\gamma\rangle_{\pm}$, where L, b, $\Delta\mu$, c and $\langle\gamma\rangle_{\pm}$ denote step length, 6.4 Å intermolecular distance along the steps, chemical potential, 3.1 Å distance between rows and step edge free energies along the + and − steps, respectively.) [36]. When the $\Delta g_{\pm}$ increases with the incorporation of Mg^{2+} into the steps, the compress stress increases and the spreading rates are inhibited.

The overgrowth compositions of calcite in Mg^{2+}-bearing solutions are also compared. Since the concentration of Mg^{2+} in calcite overgrowth is independent of precipitation rates [34], the $SI_{calcite}$ of solutions will not change Mg^{2+} contents in overgrowth. The contents of Mg^{2+} semi-quantified in our study (24.68–43.20 at%) are in accordance with Hong et al. (2016)'s calculation that the maximal Mg^{2+} content which a calcite lattice can sustain before plastic deformation is around 40 at% [37]. However, our value is greater than that obtained in a previous study using the constant disequilibrium technique (crystal-seed systems) (7–10 at%), which is attributed to the effects of the surface or adsorbed layer. As the Mg^{2+}/Ca^{2+} ratios in the surface or adsorbed layer are higher than those in the overgrowth layer, Mg^{2+} contents detected in precipitates are greater when the thickness of the overgrowth layer is extremely thin [34].

4.3.2. Aragonite Precipitation

The influence of Mg^{2+} on aragonite precipitation is a controversial topic [33,39,40], which might be partly ascribed to the limitation of research techniques in the late 20th century. These studies determined the precipitation rate by measuring weight change per unit of time, neglecting the reaction pathways. Fortunately, the in situ AFM has been successfully employed to monitor chemical reaction pathways in the past decades [3,9,16,17,20,36,37,53,55]. Our in situ AFM study discovered that the interfaces among nanoparticles formed on aragonite (110) substrates in solutions with Mg^{2+}/Ca^{2+} = 3 are more obvious than those in Mg^{2+}-free solutions, demonstrating that the precipitation rate of

aragonite is actually inhibited by Mg^{2+} through retarding the dehydration rate of precursors. However, since these previous experiments were carried out in extremely high supersaturated solutions for several hours, the inhibition of Mg^{2+} on the precipitation rate of aragonite is not easily detected on the macro-scale. According to our investigation, the aragonite precipitated on aragonite (110) substrates undergoes the oriented attachment of nanoparticles, and thus impacts of Mg^{2+} on these nanoparticles should not be ignored.

The stability of Mg^{2+} in aragonite structure directly determines overgrowth compositions. Since the coordination number of Ca^{2+} in aragonite structure is nine, Mg^{2+}, commonly occurring in six and eight coordination, cannot be preserved in aragonite for a long time. Nevertheless, a small amount of Mg^{2+} can be conserved in aragonite precursors (e.g., ACC and monoclinic aragonite, i.e., mAra), and the contents of Mg^{2+} incorporated in structures are gradually released with the transformation of mineral phases [53,60]. This prolonged precipitation provides suitable conditions for releasing Mg^{2+} from the particle precursors back into the solution, leading to low Mg^{2+} contents in the ultimate aragonite crystals (<10 at%, which is the maximum value for mAra).

4.4. Implications for the Formation of Abiogenic Carbonate Cements

Our experimental results are consistent with previous inhibition models of Mg^{2+} on the growth of calcite (104) surfaces. We discovered that the modification mechanisms of Mg^{2+} on the growth of calcite (104) and aragonite (110) substrates act on the step sites and nanoparticles, respectively, providing a new perspective on the precipitation of abiogenic $CaCO_3$ in the ocean.

It was discovered that the ACC preferentially deposits at the edges of nacreous tablets in the early stage of precipitation, and then transforms into tower-like aragonite with time [61]. This precipitation behavior of $CaCO_3$ is similar to the template effect of soluble macromolecules (SM) on $CaCO_3$ aggregation [62], which is ascribed to the change in interfacial free energy by organic templates. The regulation of organic templates on nucleation widely exists in the formation of $CaCO_3$ in vivo or on organic membranes [63,64].

In shallow marine sedimentary environments, the precipitation of $CaCO_3$ can be divided into three stages. In the first stage, phytoplankton and zooplankton produce biogenic $CaCO_3$ shells through photosynthesis and metabolism [63], respectively, belonging to direct biological regulation. When these plankton die, the precipitation of $CaCO_3$ proceeds into the second stage, in which organic membranes on these shells chiefly control the formation of $CaCO_3$ cements. After these $CaCO_3$ cements cover the majority of organic membranes, the precipitation of $CaCO_3$ enters the third stage, in which abiogenic $CaCO_3$ cements directly overgrow on the $CaCO_3$ substrate.

The findings presented in this study mainly contribute to the $CaCO_3$ precipitation in the third stage, without direct or indirect biological regulation. We observed that elongated columnar aragonite in two layers with different orientations forms on aragonite (110) surfaces, while smooth layered calcite precipitates form on calcite (104) surfaces. That is to say, the heterogeneous nucleation and growth of $CaCO_3$ on aragonite are an important origin of acicular and fibrous aragonite cements, whereas those on calcite are conducive to the formation of the secondary enlargement of calcite cements. Additionally, Mg^{2+} will inhibit the step growth of calcite and the dehydration rate of aragonite precursors, without changing the crystallization pathways of $CaCO_3$ on these two substrates, suggesting that the precipitation rate of $CaCO_3$ cements is subject to Mg^{2+}/Ca^{2+} ratios in the ocean. These discussions indicate that the distribution of different types of $CaCO_3$ in shallow-water sediments and Mg^{2+}/Ca^{2+} ratios in seawater chiefly control the formation and subsequent input flux of abiogenic $CaCO_3$ cements.

5. Conclusions

AFM, SEM, XRD and Raman analyses were utilized to investigate the heterogeneous nucleation and growth of $CaCO_3$ on calcite (104) and aragonite (110) surfaces in abiotic environments, leading to the following conclusions: (1) smooth layered calcite forms on calcite (104) surfaces; (2) elongated columnar

aragonite generated by OA of nanoparticles, aggregating along the [001] directions, precipitates on aragonite (110) surfaces; (3) Mg^{2+} inhibits the growth of aragonite and calcite formed on aragonite (110) and calcite (104) surfaces, by retarding the dehydration of precursors and blocking step growth, respectively, without affecting the crystallization pathways of $CaCO_3$ on these two substrates. The aforementioned conclusions suggest that different types of $CaCO_3$ in shallow-water sediments determine the mineralogy and morphology of abiotic $CaCO_3$ cements, and the lack of abiogenic $CaCO_3$ cements can be partly ascribed to the retardation of Mg^{2+} on the crystallization rates of both calcite and aragonite.

Supplementary Materials: The following are available online at http://www.mdpi.com/2075-163X/10/4/294/s1, Figure S1. AFM height images of the calcite (104) cleavage surfaces in solutions at Mg^{2+}/Ca^{2+} = 0 and pH = 8.0 ± 0.1 with (a) $SI_{calcite}$ = 0.50; (b) $SI_{calcite}$ = 0.83; (c) $SI_{calcite}$ = 1.05. (d) Sketch of the atomic arrangements in calcite (104) surface. The cross-section illustrates the angular relationship of the acute and obtuse step edges with terraces. And SEM image with (e) $SI_{calcite}$ = 1.05; and (f) represents the image of the red box marked zone in (e); and (g) denotes the EDS analysis of P labeled in (f). Figure S2: AFM height images of the polished aragonite (110) surface in solution (Mg^{2+}/Ca^{2+} = 0, $SI_{calcite}$ = 1.05) under flowing conditions at pH = 8.0 ± 0.1 for (a) 0, (b) 5, (c) 10, (d) 25, (e) 45 and (f) 80 min. Figure S3: AFM height images of the polished aragonite (110) surface in solution (Mg^{2+}/Ca^{2+} = 3, $SI_{calcite}$ = 1.05) under flowing conditions at pH = 8.0 ± 0.1 for (a) 0, (b) 2, (c) 5, (d) 10, (e) 20 and (f) 40 min.

Author Contributions: Conceptualization, H.T., H.X., J.Z., J.W. and H.H.; Methodology, H.T., H.X. and X.W.; Experiments, H.T., J.W. and H.L.; Data curation, H.T., H.X., J.Z. and X.W. Writing—review and editing, H.T., X.W., H.X., J.Z., J.W., H.L., and H.H. All authors have read and agreed to the published version of the manuscript.

Funding: This research was funded by the National Key R&D Program of China (Grant No. 2017YFC0602305), the National Natural Science Foundation of China (Grant No. 41825003), the Science and Technology Planning Project of Guangdong Province, China (Grant No. 2017B030314175) and the China Postdoctoral Science Foundation (Grant Nos. 2018M643220 and 2019T120755). The APC was funded by the China Postdoctoral Science Foundation (Grant No. 2019T120755).

Acknowledgments: The authors would like to thank Qin Zhou for technical assistants for SEM-EDS analysis. We are grateful to Tingting Chen, Jianlin Liao and Xin Yang for XRD analysis. We thank editors of MDPI and two anonymous reviewers who help us improve this manuscript. This is contribution No.IS-2839 from GIGCAS.

Conflicts of Interest: The authors declare no conflict of interest.

References

1. Morse, J.W.; Arvidson, R.S.; Lüttge, A. Calcium Carbonate Formation and Dissolution. *Chem. Rev.* **2007**, *107*, 342–381. [CrossRef]
2. Lasaga, A.C. *Kinetic Theory in the Earth Sciences*; Princeton University Press: Princeton, NJ, USA, 1998. Available online: https://www.jstor.org/stable/j.ctt7zvgxm (accessed on 23 March 2019).
3. Teng, H.H.; Dove, P.M.; De Yoreo, J.J. Kinetics of calcite growth: Surface processes and relationships to macroscopic rate laws. *Geochim. Cosmochim. Acta* **2000**, *64*, 2255–2266. [CrossRef]
4. Davies, G.R. Former magnesian calcite and aragonite submarine cements in upper Paleozoic reefs of the Canadian Arctic: A summary. *Geology* **1977**, *5*, 11–15. [CrossRef]
5. Kendall, A.C. Fascicular-optic calcite; a replacement of bundled acicular carbonate cements. *J. Sediment. Res.* **1977**, *47*, 1056–1062. [CrossRef]
6. Reid, R.P.; Macintyre, I.G. Carbonate recrystallization in shallow marine environments: A widespread diagenetic process forming micritized grains. *J. Sediment. Res.* **1998**, *68*, 928–946. [CrossRef]
7. Walter, L.M. Relative efficiency of carbonate dissolution and precipitation during diagenesis: A progress report on the role of solution chemistry. *Soc. Econ. Paleontol. Mineral. Spec. Publ.* **1986**, *38*, 1–12.
8. Burton, E.A.; Walter, L.M. The role of pH in phosphate inhibition of calcite and aragonite precipitation rates in seawater. *Geochim. Cosmochim. Acta* **1990**, *54*, 797–808. [CrossRef]
9. Renard, F.; Montes-Hernandez, G.; Ruiz-Agudo, E.; Putnis, C.V. Selenium incorporation into calcite and its effect on crystal growth: An atomic force microscopy study. *Chem. Geol.* **2013**, *340*, 151–161. [CrossRef]
10. Xu, M.; Riechers, S.L.; Ilton, E.S.; Du, Y.; Kovarik, L.; Varga, T.; Arey, B.W.; Qafoku, O.; Kerisit, S. Manganese-calcium intermixing facilitates heteroepitaxial growth at the (10$\bar{1}$4) calcite-water interface. *Chem. Geol.* **2017**, *470*, 152–163. [CrossRef]

11. Dobberschutz, S.; Nielsen, M.R.; Sand, K.K.; Civioc, R.; Bovet, N.; Stipp, S.L.S.; Andersson, M.P. The mechanisms of crystal growth inhibition by organic and inorganic inhibitors. *Nat. Commun.* **2018**, *9*, 1–6. [CrossRef]
12. Schott, J.; Pokrovsky, O.S.; Oelkers, E.H. The Link between Mineral Dissolution/Precipitation Kinetics and Solution Chemistry. *Rev. Mineral. Geochem.* **2009**, *70*, 207–258. [CrossRef]
13. Burton, E.A. Controls on marine carbonate cement mineralogy: Review and reassessment. *Chem. Geol.* **1993**, *105*, 163–179. [CrossRef]
14. Sunagawa, I. *Crystals: Growth, Morphology and Perfection*; Cambridge University Press: Cambridge, UK, 2005; pp. 1–308.
15. Stack, A.G.; Grantham, M.C. Growth rate of calcite steps as a function of aqueous calcium-to-carbonate ratio: Independent attachment and detachment of calcium and carbonate ions. *Cryst. Growth Des.* **2010**, *10*, 1409–1413. [CrossRef]
16. Larsen, K.; Bechgaard, K.; Stipp, S.L.S. The effect of the Ca^{2+} to CO_3^{2-} activity ratio on spiral growth at the calcite (10$\bar{1}$4) surface. *Geochim. Cosmochim. Acta* **2010**, *74*, 2099–2109. [CrossRef]
17. Sand, K.K.; Tobler, D.J.; Larsen, K.K.; Makovicky, E.; Andersson, M.P.; Stipp, S.L.S. Calcite growth kinetics: Dependence on saturation index, Ca^{2+}:CO_3^{2-}activity ratio, and surface atomic structure. *Cryst. Growth Des.* **2016**, *16*, 3602–3612. [CrossRef]
18. Gutjahr, A.; Dabringhaus, H.; Lacmann, R. Studies of the growth and dissolution kinetics of the $CaCO_3$ polymorphs calcite and aragonite II. The influence of divalent cation additives on the growth and dissolution rates. *J. Cryst. Growth* **1996**, *158*, 310–315. [CrossRef]
19. Dove, P.M.; De Yoreo, J.J.; Weiner, S. *Biomineralization: Reviews in Mineralogy and Geochemistry*; Mineralogical Society of America; Geochemical Society: Chantilly, VA, USA; Washington, DC, USA, 2003; pp. 1–377.
20. Xu, J.; Wang, J.; Hong, M.; Teng, H.H. Solution-chemistry control of Mg^{2+}-calcite interaction mechanisms: Implication for biomineralization. *Am. Mineral.* **2016**, *101*, 1104–1112. [CrossRef]
21. Mavromatis, V.; Goetschl, K.E.; Grengg, C.; Konrad, F.; Purgstaller, B.; Dietzel, M. Barium partitioning in calcite and aragonite as a function of growth rate. *Geochim. Cosmochim. Acta* **2018**, *237*, 65–78. [CrossRef]
22. Berner, R.; Westrich, J.; Graber, R.; Smith, J.; Martens, C. Inhibition of Aragonite precipitation from Supersaturated Seawater: A Laboratory and Field Study. *Am. J. Sci.* **1978**, *278*, 816–837. [CrossRef]
23. Morse, J.W.; Mucci, A. Composition of carbonate overgrowths produced on Iceland spar calcite crystals buried in Bahamian carbonate-rich sediments. *Sediment. Geol.* **1984**, *40*, 287–291. [CrossRef]
24. Lioliou, M.G.; Paraskeva, C.A.; Koutsoukos, P.G.; Payatakes, A.C. Heterogeneous nucleation and growth of calcium carbonate on calcite and quartz. *J. Colloid Interface Sci.* **2007**, *308*, 421–428. [CrossRef] [PubMed]
25. Ren, D.; Feng, Q.; Bourrat, X. Effects of additives and templates on calcium carbonate mineralization in vitro. *Micron* **2011**, *42*, 228–245. [CrossRef] [PubMed]
26. Li, Q.; Fernandez-Martinez, A.; Lee, B.; Waychunas, G.A.; Jun, Y.S. Interfacial energies for heterogeneous nucleation of calcium carbonate on mica and quartz. *Environ. Sci. Technol.* **2014**, *48*, 5745–5753. [CrossRef] [PubMed]
27. Li, Q.; Jun, Y.S. The apparent activation energy and pre-exponential kinetic factor for heterogeneous calcium carbonate nucleation on quartz. *Commun. Chem.* **2018**, *1*, 1–9. [CrossRef]
28. Lin, Y.; Hu, Q.; Chen, J.; Ji, J.; Teng, H.H. Formation of metastable $CaCO_3$ polymorphs in the presence of oxides and silicates. *Cryst. Growth Des.* **2009**, *9*, 4634–4641. [CrossRef]
29. Xu, H.; Zhou, M.; Fang, Y.; Teng, H.H. Effect of mica and hematite (001) surfaces on the precipitation of calcite. *Minerals* **2018**, *8*, 17. [CrossRef]
30. Sun, W.; Jayaraman, S.; Chen, W.; Persson, K.A.; Ceder, G. Nucleation of metastable aragonite $CaCO_3$ in seawater. *Proc. Natl. Acad. Sci. USA* **2015**, *112*, 3199–3204. [CrossRef]
31. Li, L.; Fijneman, A.J.; Kaandorp, J.A.; Aizenberg, J.; Noorduin, W.L. Directed nucleation and growth by balancing local supersaturation and substrate/nucleus lattice mismatch. *Proc. Natl. Acad. Sci. USA* **2018**, *115*, 3575–3580. [CrossRef]
32. Bathurst, R.G. Diagenetically enhanced bedding in argillaceous platform limestones: Stratified cementation and selective compaction. *Sedimentology* **1987**, *34*, 749–778. [CrossRef]
33. Berner, R.A. The role of magnesium in the crystal growth of calcite and aragonite from sea water. *Geochim. Cosmochim. Acta* **1975**, *39*, 489–504. [CrossRef]

34. Mucci, A.; Morse, J.W. The incorporation of Mg^{2+} and Sr^{2+} into calcite overgrowths: Influences of growth rate and solution composition. *Geochim. Cosmochim. Acta* **1983**, *47*, 217–233. [CrossRef]
35. Zhong, S.; Mucci, A. Calcite and aragonite precipitation from seawater solutions of various salinities: Precipitation rates and overgrowth compositions. *Chem. Geol.* **1989**, *78*, 283–299. [CrossRef]
36. Teng, H.H.; Dove, P.M.; Orme, C.A.; Yoreo, J.J.D. Thermodynamics of Calcite Growth: Baseline for Understanding Biomineral Formation. *Science* **1998**, *282*, 724–727. [CrossRef] [PubMed]
37. Hong, M.; Xu, J.; Teng, H.H. Evolution of calcite growth morphology in the presence of magnesium: Implications for the dolomite problem. *Geochim. Cosmochim. Acta* **2016**, *172*, 55–64. [CrossRef]
38. Sinha, S.; Rez, P. Distortions of the calcite and aragonite atomic structures from interstitial water. *Mater. Chem. Phys.* **2015**, *157*, 56–62. [CrossRef]
39. Pytkowicz, R.M. Rates of inorganic calcium carbonate nucleation. *J. Geol.* **1965**, *73*, 196–199. [CrossRef]
40. Lippmann, F. *Sedimentary Carbonate Minerals*; Springer: Berlin/Heidelberg, Germany, 1973; pp. 1–233.
41. Gustafsson, J.P. *Visual MINTEQ 3.0 User Guide*; KTH, Department of Land and Water Recources: Stockholm, Sweden, 2011. Available online: http://www2.lwr.kth.se/English/OurSoftware/vminteq/contact.html (accessed on 20 March 2012).
42. Tang, H.; Xian, H.; He, H.; Wei, J.; Liu, H.; Zhu, J.; Zhu, R. Kinetics and mechanisms of the interaction between the calcite (10.4) surface and Cu^{2+}-bearing solutions. *Sci. Total Environ.* **2019**, *668*, 602–616. [CrossRef]
43. Van Driessche, A.E.; Kellermeier, M.; Benning, L.G.; Gebauer, D. *New Perspectives on Mineral Nucleation and Growth: From Solution Precursors to Solid Materials*; Springer: Cham, Switzerland, 2016; pp. 1–380.
44. De Yoreo, J.J.; Gilbert, P.U.P.A.; Sommerdijk, N.A.J.M.; Penn, R.L.; Whitelam, S.; Joester, D.; Zhang, H.; Rimer, J.D.; Navrotsky, A.; Banfield, J.F.; et al. Crystallization by particle attachment in synthetic, biogenic, and geologic environments. *Science* **2015**, *349*, 498–507. [CrossRef]
45. Gránásy, L.; Pusztai, T.; Tegze, G.; Warren, J.A.; Douglas, J.F. Growth and form of spherulites. *Phys. Rev. E* **2005**, *72*, 11605. [CrossRef]
46. Cubillas, P.; Köhler, S.; Prieto, M.; Causserand, C.; Oelkers, E.H. How do mineral coatings affect dissolution rates? An experimental study of coupled $CaCO_3$ dissolution—$CdCO_3$ precipitation. *Geochim. Cosmochim. Acta* **2005**, *69*, 5459–5476. [CrossRef]
47. Zhou, G.T.; Yao, Q.Z.; Ni, J.; Jin, G. Formation of aragonite mesocrystals and implication for biomineralization. *Am. Mineral.* **2009**, *94*, 293–302. [CrossRef]
48. Nielsen, M.H.; Aloni, S.; De Yoreo, J.J. In situ TEM imaging of $CaCO_3$ nucleation reveals coexistence of direct and indirect pathways. *Science* **2014**, *345*, 1158–1162. [CrossRef] [PubMed]
49. Walker, J.M.; Marzec, B.; Nudelman, F. Solid-State Transformation of Amorphous Calcium Carbonate to Aragonite Captured by CryoTEM. *Angew. Chem. Int. Edit.* **2017**, *56*, 11740–11743. [CrossRef] [PubMed]
50. Alberstein, R.G.; Tezcan, F.A. Observations of the birth of crystals. *Nature* **2018**, *556*, 41–42. [CrossRef] [PubMed]
51. Sethmann, I.; Wang, J.; Becker, U.; Putnis, A. Strain-induced segmentation of magnesian calcite thin films growing on a calcite substrate. *Cryst. Growth Des.* **2010**, *10*, 4319–4326. [CrossRef]
52. Shannon, R.D. Revised effective ionic-radii and systematic studies of interatomic distances in halides and chalcogenides. *Acta Crystallogr. Sect. A.* **1976**, *32*, 751–767. [CrossRef]
53. Elhadj, S.; De Yoreo, J.J.; Hoyer, J.R.; Dove, P.M. Role of molecular charge and hydrophilicity in regulating the kinetics of crystal growth. *Proc. Natl. Acad. Sci. USA* **2006**, *103*, 19237–19242. [CrossRef]
54. Nemeth, P.; Mugnaioli, E.; Gemmi, M.; Czuppon, G.; Demeny, A.; Spoetl, C. A nanocrystalline monoclinic $CaCO_3$ precursor of metastable aragonite. *Sci. Adv.* **2018**, *4*, eaau6178. [CrossRef]
55. Wasylenki, L.E.; Dove, P.M.; Wilson, D.S.; De Yoreo, J.J. Nanoscale effects of strontium on calcite growth: An in situ AFM study in the absence of vital effects. *Geochim. Cosmochim. Acta* **2005**, *69*, 3017–3027. [CrossRef]
56. Teng, H.H.; Dove, P.M.; DeYoreo, J.J. Reversed calcite morphologies induced by microscopic growth kinetics: Insight into biomineralization. *Geochim. Cosmochim. Acta* **1999**, *63*, 2507–2512. [CrossRef]
57. De Yoreo, J.J.; Vekilov, P.G. Principles of crystal nucleation and growth. In *Biomineralization: Reviews in Mineralogy and Geochemistry*; Mineralogical Society of America; Geochemical Society: Chantilly, VA, USA; Washington, DC, USA, 2003; Volume 54, pp. 57–93.
58. Davis, K.J.; Dove, P.M.; De Yoreo, J.J. The role of Mg^{2+} as an impurity in calcite growth. *Science* **2000**, *290*, 1134–1137. [CrossRef] [PubMed]

59. Astilleros, J.; Fernández-Díaz, L.; Putnis, A. The role of magnesium in the growth of calcite: An AFM study. *Chem. Geol.* **2010**, *271*, 52–58. [CrossRef]
60. Mass, T.; Giuffre, A.J.; Sun, C.Y.; Stifler, C.A.; Frazier, M.J.; Neder, M.; Tamura, N.; Stan, C.V.; Marcus, M.A.; Gilbert, P.U. Amorphous calcium carbonate particles form coral skeletons. *Proc. Natl. Acad. Sci. USA* **2017**, *114*, 7670–7678. [CrossRef]
61. Luo, C.; Xie, L.; Wang, X.X. In vitro growth of aragonite crystal on nacre surface. *Key Eng. Mat.* **2007**, *330*, 1335–1338. [CrossRef]
62. Gal, A.; Wirth, R.; Kopka, J.; Fratzl, P.; Faivre, D.; Scheffel, A. Macromolecular recognition directs calcium ions to coccolith mineralization sites. *Science* **2016**, *353*, 590–593. [CrossRef] [PubMed]
63. Branson, O.; Bonnin, E.A.; Perea, D.E.; Spero, H.J.; Zhu, Z.; Winters, M.; Hönisch, B.; Russell, A.D.; Fehrenbacher, J.S.; Gagnon, A.C. Nanometer-scale chemistry of a calcite biomineralization template: Implications for skeletal composition and nucleation. *Proc. Natl. Acad. Sci. USA* **2016**, *113*, 12934–12939. [CrossRef]
64. Gal, A.; Wirth, R.; Barkay, Z.; Eliaz, N.; Scheffel, A.; Faivre, D. Templated and self-limiting calcite formation directed by coccolith organic macromolecules. *Chem. Commun.* **2017**, *53*, 7740–7743. [CrossRef]